

# Measurement of the scintillation efficiency for nuclear recoils in liquid argon under electric fields up to 3 kV/cm

M.Kimura,\* M.Tanaka, T.Washimi,<sup>†</sup> and K.Yorita<sup>‡</sup>  
*Waseda University, 3-4-1, Okubo, Shinjuku, Tokyo, 169-8555, Japan*  
(Dated: July 28, 2022)

We present a measurement of scintillation efficiency for a few tens of keV nuclear recoils (NR) with liquid argon time projection chamber under electric fields ranging from 0 to 3 kV/cm. The calibration data is taken with  $^{252}\text{Cf}$  radioactive source. Observed scintillation (S1) and electroluminescence (S2) spectra are simultaneously fit with spectra derived from Geant4-based Monte Carlo simulation and an NR model. The scintillation efficiency extracted from the fit is reported as a function of recoil energy and electric field. This result can be used for designing the detector and for the interpretation of experimental data in searching for scintillation and ionization signals induced by WIMP dark matter.

## I. INTRODUCTION

Dark matter appears to be spread across galaxies through astronomical and cosmological observations, and many groups have been trying to detect it directly using a variety of detector techniques and target materials. There are many direct detection experiments to identify nuclear recoils (NR) induced by elastic scattering of weakly interacting massive particle (WIMP) off target nuclei. The magnitude of the typical recoil energy in these experiments is a few tens of keV. Liquid argon (LAr) time projection chamber (TPC) is known to offer several attractive features to search for WIMP with mass in GeV to TeV range [1–5]: efficient conversion of energy deposition into scintillation and ionization signals, powerful discrimination of NR signal from electronic recoils (ER) background, and reasonably high recoil energy for WIMP-Ar nuclear scattering due to relatively small atomic mass of argon. In the double-phase (liquid/gas) TPC, excitation and ionization are induced by an incident particle after interacting with LAr, leading to prompt scintillation signal (S1). Active volume of the detector is subjected to a uniform electric field, which causes ionization electrons to escape recombination and drift toward the gaseous region, where they emit electroluminescence signal (S2). It is known that light and charge yields, i.e., the number of scintillation photons and the number of ionization electrons, respectively, produced by an NR of a given energy, depend on both the energy and applied electric field. The scintillation efficiency  $\mathcal{L}_{\text{eff}}$  is defined as the light yield for NR per recoil energy relative to that of ER measured at null field. Although it has been measured by several groups [6–11], the properties for electric fields greater than 1 kV/cm have not been explicitly discussed yet. In this work, we report the first measurement of the scintillation efficiency

$\mathcal{L}_{\text{eff}}$  resulting from a few tens of keV of NR under electric fields up to 3 kV/cm.

## II. NUCLEAR RECOILS MODEL

### A. Framework

The observable quantities in the double-phase LAr-TPC are S1 and S2 light signals. A schematic for the conversion process of NR energy into these observable quantities is shown in Fig. 1. An energy deposition of  $E_0$  from NR is distributed as expressed in the following equation :

$$\frac{E_0 L}{W} = N_{\text{ex}} + N_i = N_i(\alpha + 1) \quad (1)$$

where  $W = 19.5$  eV is the effective work function [12],  $L$  is an additional factor that accounts for energy loss due to atomic motion,  $N_{\text{ex}}$  and  $N_i$  are the average number of produced excitons and electron-ion pairs, respectively, and  $\alpha$  is the exciton-to-ion ratio. The factor  $L$  is predicted using Lindhard theory [13] as follows:

$$\begin{aligned} L &= \frac{kg(\epsilon)}{1 + kg(\epsilon)}, \\ k &= 0.133Z^{2/3}A^{-1.2}, \\ g(\epsilon) &= 3\epsilon^{0.15} + 0.7\epsilon^{0.6} + \epsilon, \\ \epsilon &= 11.5(E_0/\text{keV})Z^{-7/3}, \end{aligned} \quad (2)$$

where  $Z = 18$  and  $A = 40$  are the atomic and mass numbers, respectively. The ratio  $\alpha$  is parameterized as an empirical function of electric field  $F$ , similar to the description for liquid xenon in Ref. [14],

$$\alpha = \alpha_0 \exp(-D_\alpha F), \quad (3)$$

where  $\alpha_0$  and  $D_\alpha$  are free parameters. Once the energy deposition is distributed to ionization, excitation, or atomic motion channels, all the excitons contribute directly to the emission of scintillation photons. A fraction of electrons recombines with ions to produce additional

\* masato@kylab.sci.waseda.ac.jp

<sup>†</sup> Present address: High Energy Accelerator Research Organization (KEK)

<sup>‡</sup> kohei.yorita@waseda.jp

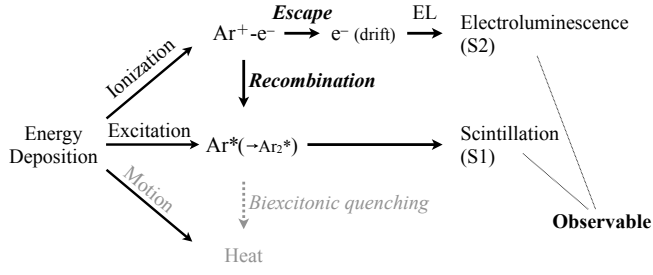


FIG. 1. Nuclear recoils model.

scintillation photons, whereas the rest of the electrons become ionization electrons. The electrons drift toward the gaseous region and emit electroluminescence. An empirical modification [15] of the Thomas-Imel box model (TIB model) [16] provides the recombination probability  $R$  as follows:

$$R = 1 - \frac{\ln(1 + N_i \varsigma)}{N_i \varsigma}, \quad (4)$$

$$\varsigma = \gamma F^{-\delta}.$$

Here,  $\gamma$  and  $\delta$  are free parameters. Biexcitonic quenching, where a collision of two excitons produces a single photon, is incorporated by Mei model [17]. The quenching term  $f_l$  is parameterized by

$$f_l = \frac{1}{1 + k_B \left( \frac{dE}{dx} \right)_{\text{el}}}, \quad (5)$$

where  $k_B$  is a free parameter. The electronic stopping power  $(\frac{dE}{dx})_{\text{el}}$  is given by Mei *et al.* as a function of the recoil energy  $E_0$  (Fig. 5 in Ref. [17]). Summarizing these effects, the number of produced scintillation photons,  $n_{ph}$ , and the number of produced ionization electrons,  $n_e$ , are expressed as follows:

$$n_{ph} = L \times f_l \times \frac{E_0}{W} \times \left[ 1 - \left( \frac{1}{1 + \alpha} \right) (1 - R) \right], \quad (6)$$

$$n_e = L \times \frac{E_0}{W} \times \left( \frac{1}{1 + \alpha} \right) (1 - R). \quad (7)$$

These quantities are related to S1 and S2 as follows:

$$S1 = g_1 n_{ph}, \quad (8)$$

$$S2 = g_2 n_e, \quad (9)$$

where  $g_1$  is the scintillation photon collection efficiency and  $g_2$  is the average number of detected electroluminescence photons per one drift electron. Both  $g_1$  and  $g_2$  are considered as detector properties and remain constant for NR and ER events.

## B. Fitting procedure

For NR at null field,  $R$  is expected to be 1; therefore,  $k_B$  is the only free parameter to account for the

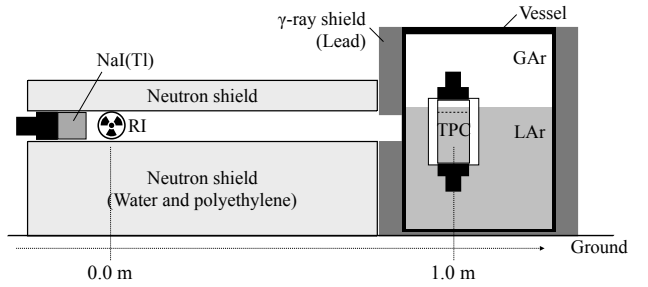


FIG. 2. Schematic of the experimental apparatus.

quenching. As applying the electric field,  $R$  is expected to decrease, resulting in the suppression of S1 signal and production of more S2 signal. The related parameters of this process are  $\alpha_0$ ,  $D_\alpha$ ,  $\gamma$ , and  $\delta$  in Eqs. (3) and (4). In the previous measurements of the light yields, a value of  $\alpha \sim 1$  is suggested to describe the observed data [8, 11]. We interpret the value to the approximation at the lower electric field, and constrain  $\alpha_0$  to 1. We first determine  $k_B$  from the S1 spectrum of the null field data sample, and then  $D_\alpha$ ,  $\gamma$ , and  $\delta$  are obtained from both S1 and S2 spectra under electric fields.

In this measurement, 511 keV  $\gamma$ -ray line from  $^{22}\text{Na}$  source is used as the reference ER events of the scintillation efficiency  $\mathcal{L}_{\text{eff}}$ . For ER at null field,  $L = f_l = 1$  and  $R = 1$  are expected. Therefore, the observed S1 light signal ( $S1_{\text{Na}}$ ) by energy deposition of  $E_{\text{Na}} = 511$  keV from ER at null field is represented as following:

$$S1_{\text{Na}} = g_1 \frac{E_{\text{Na}}}{W}. \quad (10)$$

A value of  $g_1 = 0.12 \pm 0.01$  is measured in this work that will be described in Sec. III B. We derived  $g_2/g_1$  value by analyzing the ER data samples under electric fields that were taken by the same experimental condition [18]. A value of  $g_2/g_1 = 10 \pm 2$  is obtained and used as the detector constants.

## III. APPARATUS

### A. Detector and geometry

We measured the scintillation efficiency at LAr test stand at Waseda University [19]. The double-phase TPC used in this study has an active region of diameter 6.4 cm and height 10 cm with two PMTs (HAMAMATSU R11065). An extraction grid is placed at the top of the active region. The gap between the extraction grid and anode is 1 cm, and liquid surface is kept centered between them. A Cockcroft-Walton circuit is mounted in the LAr that surrounds the TPC to supply high voltage to the electrodes of TPC. Data were taken under electric fields of 0.0, 0.2, 0.5, 1.0, 2.0, and 3.0 kV/cm. More details are described elsewhere [19–21].

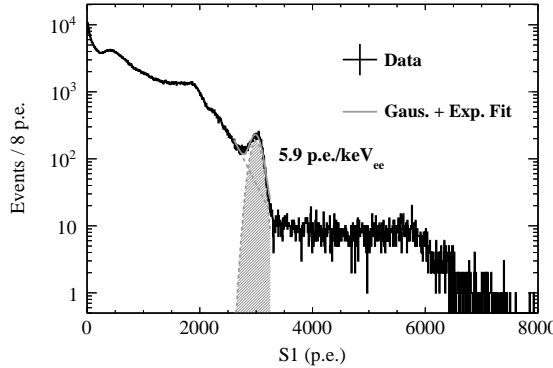


FIG. 3.  $^{22}\text{Na}$  spectrum for energy calibration at null field, with the Gaussian plus exponential fitting around 511 keV full absorption peak.

Figure 2 shows a schematic of the experimental apparatus used in this measurement.  $^{252}\text{Cf}$  neutron source with radioactivity of approximately 3 MBq is placed at a distance of  $1.01 \pm 0.01$  m from the center of the TPC. An NaI(Tl) scintillator (2 inch  $\times$  2 inch cylinder) located beside the neutron source provides timing information by detecting associated  $\gamma$ -ray. Lead shield surrounds the vessel to suppress background from ambient  $\gamma$ -rays. Other background arises because of neutrons from the  $^{252}\text{Cf}$  source; this background from the  $^{252}\text{Cf}$  source reaches the active region via single or multiple scattering at any part of materials in the laboratory. Water and polyethylene shields are placed to suppress these scattered neutrons. The data acquisition is triggered by coincidence between the TPC PMTs and NaI(Tl) scintillator signals within a 1  $\mu\text{s}$  window. Both TPC PMT and NaI(Tl) scintillator waveforms are digitized at a frequency of 250 MHz using a flash ADC (SIS3316). The length of the digitizer records is set to long enough to detect S2 of the maximum drift (10 cm) events.

### B. Energy calibration of TPC

Figure 3 shows the S1 spectrum of the  $^{22}\text{Na}$  data taken at null field. We determine the observed S1 signal per ER energy at null field,  $S1_{\text{Na}}/E_{\text{Na}}$ , as  $5.9 \pm 0.3$  p.e./keV<sub>ee</sub> (p.e.: photo-electron, ee: electron equivalent) by fitting 511 keV full absorption peak with Gaussian plus exponential function. The corresponding scintillation photon collection efficiency  $g_1$  of the detector is  $0.12 \pm 0.01$ .

### IV. EVENT RECONSTRUCTION

The energy of the incident neutron from the  $^{252}\text{Cf}$  source is reconstructed based on time of flight (TOF), i.e., the time difference between the NaI(Tl) and TPC signals. The arrival time of a pulse is identified as the

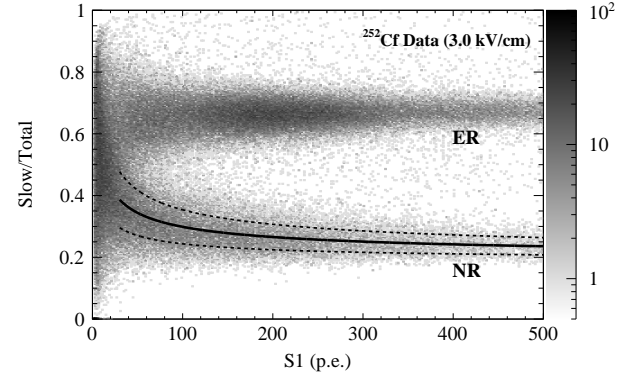


FIG. 4. Distribution of the PSD parameter (Slow/Total) versus S1 with data taken with the  $^{252}\text{Cf}$  neutron source under the electric field of 3 kV/cm. Two dashed lines correspond to the band for PSD cut ( $\pm 1\sigma$ ).

first digitized sample above a threshold of 50% peak amplitude. The S1 is reconstructed as integrated charge in the time interval between  $-0.04$  and  $5.0$   $\mu\text{s}$ . Pulse shape discrimination (PSD) parameter Slow/Total is defined as the fraction of light detected after  $0.12$   $\mu\text{s}$  of S1 signal. The S2 is reconstructed as integrated charge after  $10$   $\mu\text{s}$  in the data acquisition window. Events of the data samples are selected by requiring one proper S1 pulse. For data samples taken under the electric fields, the additional requirement to have one proper S2 pulse is applied to select single scattered NR events. Figure 4 shows a distribution of the PSD parameter (Slow/Total) versus S1 with data taken under the electric field of 3 kV/cm, after requiring the TOF to be in the range of 43–111 ns, corresponding to incident neutron energy of 0.41–2.44 MeV. The neutrons from the  $^{252}\text{Cf}$  source can induce  $\gamma$ -ray through interaction with passive detector materials. These induced  $\gamma$ -rays are observed to result in ER events having neutron-like timing. Thus PSD band cut ( $\pm 1\sigma$ ) is imposed to select NR events and suppress ER contamination. Contribution from accidental coincidence backgrounds is estimated from negative TOF window of  $-0.9$  to  $-0.2$   $\mu\text{s}$ .

## V. METHOD

### A. Monte Carlo

Energy deposits by the neutrons are simulated in a Geant4-based [22, 23] Monte Carlo (MC) of the experimental apparatus, using neutron spectrum of  $^{252}\text{Cf}$  in Ref. [24] and nuclear data library files G4NDL 4.5 [25–27] with an revised differential cross sections for elastic scattering from Ref. [28]. We confirmed the validity of the simulation using comparison of the TOF distribution between data and MC in Fig. 5. The observed events in data at around TOF = 0 s mainly consist of low-energy

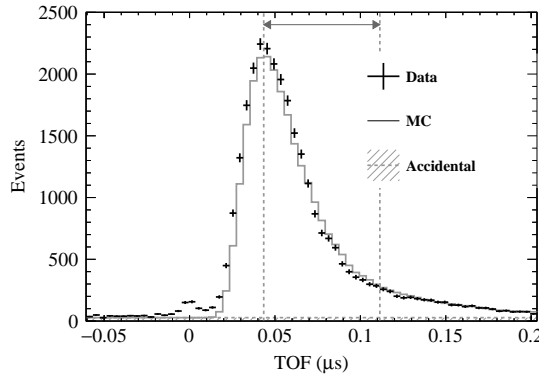


FIG. 5. Comparison between data and MC TOF spectra. The vertical dashed lines and gray arrow represent the TOF range where the simultaneous fit is performed. Contamination from ER events that are not simulated in MC produces the peak around 0 s.

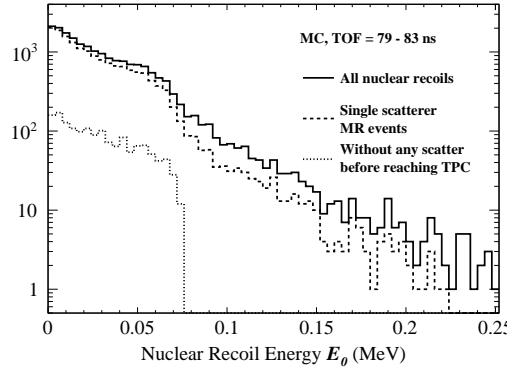


FIG. 6. Energy deposition spectra derived from Geant4-based MC simulation. Shown are all NR in the LAr active region (solid line), contributions from single scattered NR events (i.e., neutrons that scattered only once in the active region) (dashed line), and neutrons that reached without any scattering in any part of the apparatus before reaching the active region (dotted line).

$(S1 \lesssim 30 \text{ p.e.})$  events. These events are considered as contamination from ER events and not used in this analysis. Figure 6 shows energy deposition ( $E_0$ ) distribution from the MC for the TOF range of 79–83 ns, corresponding to neutron energy of about 0.75 MeV. While the  $^{252}\text{Cf}$  source has a continuous neutron spectrum, a back-scatter edge would be visible by constraining the TOF. The edge of each TOF bin is useful to resolve degeneracy between the free parameters as described later. The leading contribution is expected from the neutrons that are scattered more than once in any part of the apparatus (such as neutron/gamma shieldings, vessel, and LAr that surrounds the TPC) before reaching the active region. However, the position of the back-scatter edge is not affected, as shown in Fig. 6.

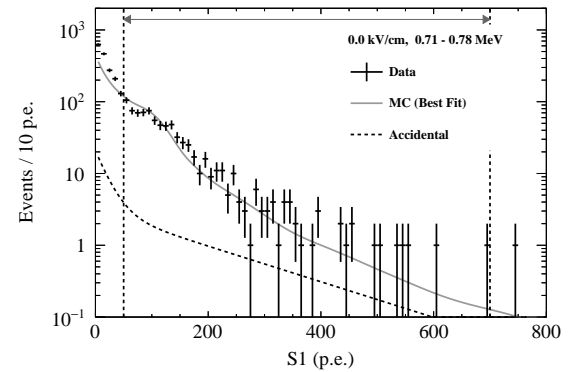


FIG. 7. S1 spectrum of the NR data sample taken at null field and MC-derived spectrum simultaneously fitted to experimental data for TOF in the range of 79–83 ns. The area indicated by vertical dashed lines and gray arrow represent the fitting range.

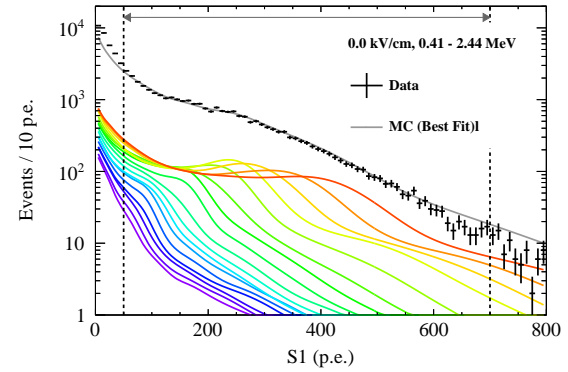


FIG. 8. S1 spectrum of the NR data sample taken at null field (black point) and MC-derived spectrum simultaneously fitted to experimental data (gray line) for the entire TOF range of interest. Also shown are MC-derived spectra (colored lines) representing the contribution of each TOF bin, from 43–47 ns (red) to 107–111 ns (violet). The area indicated by vertical dashed lines and gray arrow represent the fitting range.

## B. Data fitting

The parameters in the NR model are measured by fitting the obtained S1 and S2 spectra of each TOF bin (4 ns interval) with the spectra derived from the MC and the NR model described in Sec. II. The fit is simultaneously performed in the TOF range of 43–111 ns (total 17 TOF bins). The MC spectra of both S1 and S2 are convolved with Gaussian resolution functions. Figure 7 shows an example of the S1 spectrum and the fitted MC spectrum for a TOF bin of 79–83 ns at null field. Figure 8 shows the spectrum for the entire TOF range of interest with the 17 MC spectra for each TOF bin. Figure 9 shows an example of the S1 and S2 spectra and the fitted MC

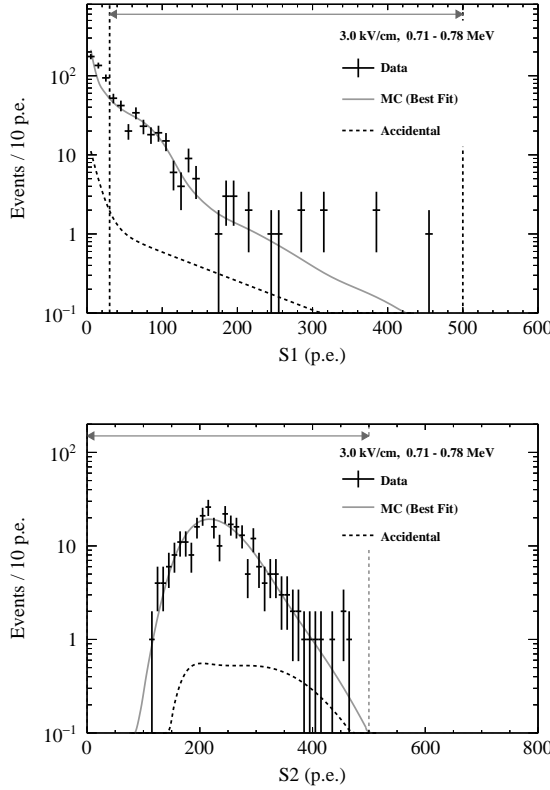


FIG. 9. S1 (top) and S2 (bottom) spectra of the NR data sample taken at the electric field of 3.0 kV/cm and MC-derived spectra simultaneously fitted to experimental data for TOF in the range of 79–83 ns. The area indicated by vertical dashed lines and gray arrow represent the fitting range.

spectra for a TOF bin of 79–83 ns under the electric field of 3 kV/cm. The spectra for the entire TOF range of interest with the respective 17 MC spectra is shown in Fig. 10. We should note that since the spectra for the entire TOF range of interest have smooth spectrum shape, as shown in Figs. 8 and 10, it is difficult to uniquely resolve the degeneracy between the free parameters by the inclusive shape. However, the back-scatter edge of each TOF bin makes it possible to access each parameter. This is because the edges characterize a light and charge yield dependency on the NR energy. We also note that the fit range of S2 spectra is constrained to below 500 p.e. as the discrepancy between data and MC is observed above 500 p.e. This discrepancy is presumably due to the multiple scattered events that survive the event selections mentioned above.

A consistency check of the fit is performed by predicting  $\log_{10}(S2/S1)$  value for the entire TOF range for  $^{252}\text{Cf}$  neutron events. Figure 11 shows the  $^{252}\text{Cf}$  data for all the five values of electric field with an overlay of the prediction (shown by solid line) from the fit parameters in  $\log_{10}(S2/S1)$  versus S1 plane. Reasonable agreements of mean value of the  $\log_{10}(S2/S1)$  distributions are achieved

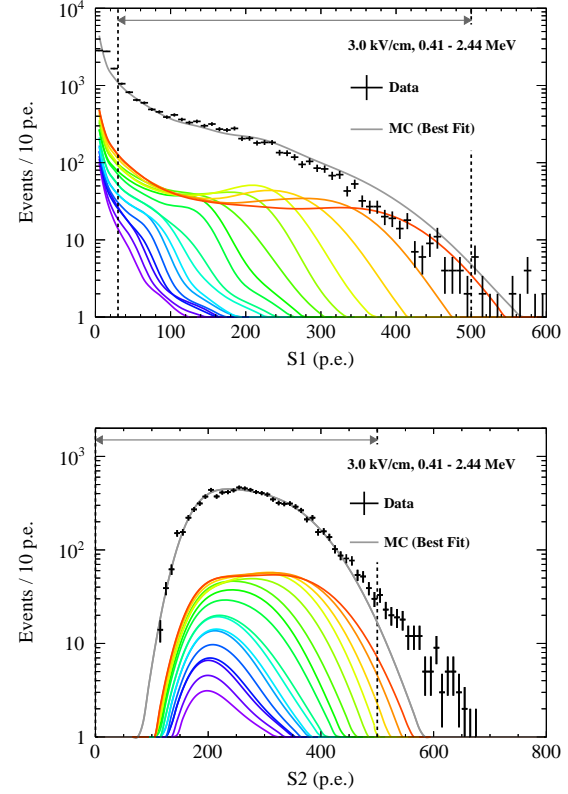


FIG. 10. S1 (top) and S2 (bottom) spectra of the NR data sample taken at the electric field of 3.0 kV/cm and MC-derived spectra simultaneously fitted to experimental data for the entire TOF range of interest. The figure description is the same as in Fig. 8.

TABLE I. Results from the simultaneous fit of  $^{252}\text{Cf}$  data with the MC simulation and the NR model described in Sec. II.

Parameter	Value
$k_B$ [g/(MeV · cm $^2$ )]	$3.1 \times 10^{-4}$
$\alpha_0$ (fixed)	1.0
$D_\alpha$ [(V/cm) $^{-1}$ ]	$9.2 \times 10^{-4}$
$\gamma$ [(V/cm) $^\delta$ ]	1.2
$\delta$	$5.7 \times 10^{-1}$

at all the five electric fields.

## VI. RESULT

The best fit values of the NR model are summarized in Tab. I. The scintillation efficiency  $\mathcal{L}_{\text{eff}}$  is the ratio of the light yield for NR events per recoil energy to that for ER events by definition. Therefore, from Eqs. (6), (8), and (10), the scintillation efficiency  $\mathcal{L}_{\text{eff}}$  referenced

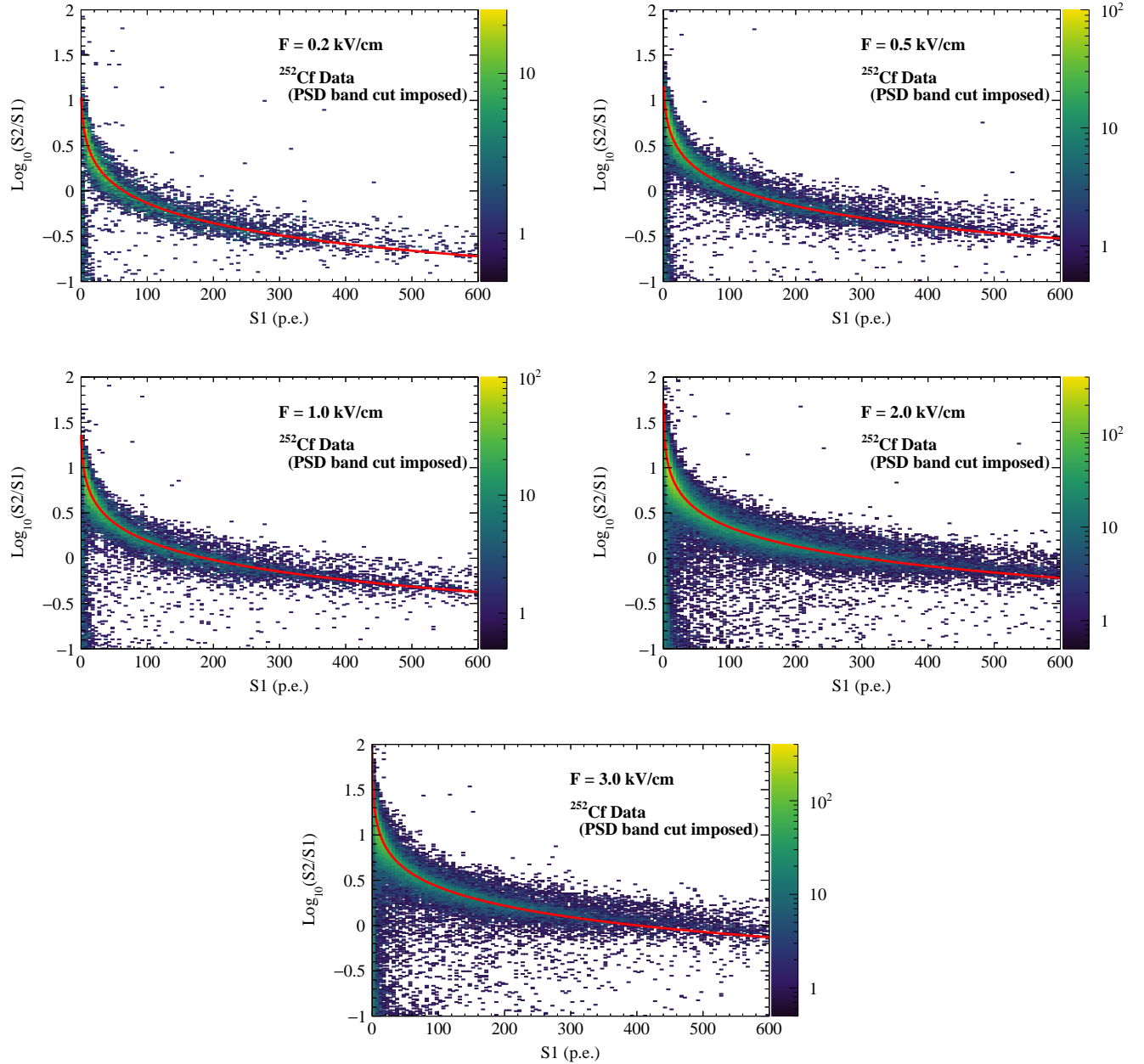


FIG. 11.  $^{252}\text{Cf}$  data taken with the electric fields of 0.2, 0.5, 1.0, 2.0, and 3.0 kV/cm (from left to right and top to bottom) in  $\log_{10}(S2/S1)$  versus  $S1$  plane, overlaid with the prediction from the NR model and the best fit parameters (solid line).

to 511 keV  $\gamma$ -ray line of  $^{22}\text{Na}$  source is given by

$$\mathcal{L}_{\text{eff}}(E_0, F) = \frac{(S1/E_0)}{(S1_{\text{Na}}/E_{\text{Na}})} = \frac{n_{ph}}{E_0/W}. \quad (11)$$

The  $\mathcal{L}_{\text{eff}}$  dependency on the NR energy and the electric field is shown in Fig. 12 in comparison with the previous measurements by other groups [8, 10, 11]. An energy threshold of this measurement is set to 30 keV, for which we constrained the fit range of  $S1$  spectra where there is sufficient PSD power to extract pure NR events. Due to the poor statistics of high energy NR events, an up-

per 200 keV boundary is also set. The NR model can be extrapolated to both lower and higher energy region as represented with dashed lines in Fig. 12. Each result on the  $\mathcal{L}_{\text{eff}}$  value has the total uncertainty of 0.02, as indicated with black error bar. The dominant contributions to the uncertainty are the systematic uncertainty from the energy calibration of the detector, the value of  $g_2/g_1$ , and the distance between TPC and  $^{252}\text{Cf}$  source. The statistical uncertainty is about 10% of the systematic uncertainty. Since scintillation response in LAr for ER in the range 41.5–511 keV at null field is constant within

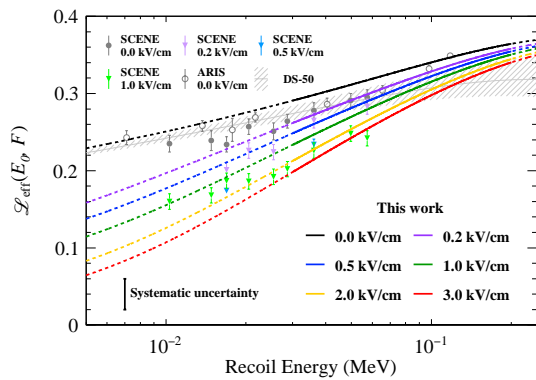


FIG. 12. Scintillation efficiency  $\mathcal{L}_{\text{eff}}$  as a function of the NR energy measured in this work. Uncertainty in  $\mathcal{L}_{\text{eff}}$ , as indicated as black error bar in the plot, applies to all field points. Measurements from SCENE [8], ARIS [11], and DarkSide-50 (DS-50) [10] are also shown.

1.6% [11], the result can be subjected to the comparison with other  $\mathcal{L}_{\text{eff}}$  measurements using different reference sources (such as  $^{83m}\text{Kr}$  [8] or  $^{241}\text{Am}$  [11]). Although we are not aware of any theoretical description about the empirical field dependency of  $\alpha$ , yet it is consistent with our data samples.

## VII. CONCLUSION

The scintillation efficiency of LAr for NR ranging from 30 to 200 keV relative to 511 keV ER is systematically measured under electric fields from 0 to 3 kV/cm using a small size double-phase TPC and a  $^{252}\text{Cf}$  radioactive source. In this measurement, observed S1 and S2 spectra are simultaneously fit with the simulated energy deposits by taking into account correlations between the light and charge yields. The parameterization model we employ in

this paper is based on existing models (Mei model and TIB model) described by the function of recoil energy and electric field. As a result, the scintillation efficiency  $\mathcal{L}_{\text{eff}}$  is successfully modeled up to 3 kV/cm within systematic uncertainty. For lower ( $F \leq 1$  kV/cm) electric field, we confirm consistency with previous measurements [8, 10, 11], while it provides new information for higher ( $F > 1$  kV/cm) electric field for the first time.

In the field of WIMP dark matter search experiments, the scintillation efficiency and the charge yield are essential parameters to convert from observed S1 and S2 signals to recoil energy by WIMP-Ar scattering. Thus comprehensive parameterization of LAr property reported in this work makes use of interpretation between the experimental data and physics process under various electric fields, and also can contribute to better understand systematic uncertainty for low energy signal region in the search. Furthermore, not only WIMP search, these results would be also useful for other physics experiments [29–31] where understandings of LAr property is necessary and play important role for obtaining physics outcomes.

## ACKNOWLEDGMENTS

The authors would like to thank Alan E. Robinson for helpful comment on the Geant4 simulation and its nuclear data library files. This work is a part of the outcome of research performed under the Waseda University Research Institute for Science and Engineering (project number 2016A-507), supported by JSPS Grant-in-Aid for Scientific Research on Innovative Areas (15H01038/17H05204), Grant-in-Aid for Scientific Research(B) (18H01234), and Grant-in-Aid for JSPS Research Fellow (18J13018). The authors acknowledge the support by Institute for Advanced Theoretical and Experimental Physics, Waseda University.

- 
- [1] P. Benetti, R. Acciari, F. Adamo, B. Baibussinov, M. Baldo-Ceolin, M. Bellucco, F. Calaprice, E. Calligarich, M. Cambiaghi, F. Carbonara, et al., *Astroparticle Phys.* **28**, 495 (2008), ISSN 0927-6505, URL <http://www.sciencedirect.com/science/article/pii/S0927650507001016>.
- [2] P.-A. Amaudruz, M. Baldwin, M. Batygov, B. Beltran, C. E. Bina, D. Bishop, J. Bonatt, G. Boorman, M. G. Boulay, B. Broerman, et al. (DEAP-3600 Collaboration), *Phys. Rev. Lett.* **121**, 071801 (2018), URL <https://link.aps.org/doi/10.1103/PhysRevLett.121.071801>.
- [3] P. Agnes, I. F. M. Albuquerque, T. Alexander, A. K. Alton, G. R. Araujo, M. Ave, H. O. Back, B. Baldin, G. Batignani, K. Biery, et al. (DarkSide Collaboration), *Phys. Rev. D* **98**, 102006 (2018), URL <https://link.aps.org/doi/10.1103/PhysRevD.98.102006>.
- [4] P. Agnes, I. F. M. Albuquerque, T. Alexander, A. K. Alton, G. R. Araujo, D. M. Asner, M. Ave, H. O. Back, B. Baldin, G. Batignani, et al. (DarkSide Collaboration), *Phys. Rev. Lett.* **121**, 081307 (2018), URL <https://link.aps.org/doi/10.1103/PhysRevLett.121.081307>.
- [5] R. Ajaj, P.-A. Amaudruz, G. Araujo, M. Baldwin, M. Batygov, B. Beltran, C. Bina, J. Bonatt, M. Boulay, B. Broerman, et al. (DEAP Collaboration), *Search for dark matter with a 231-day exposure of liquid argon using deap-3600 at snolab*, e-print arXiv:astro-ph.CO/1902.04048 (2019).
- [6] R. Brunetti, E. Calligarich, M. Cambiaghi, F. Carbonara, A. Cocco, C. D. Vecchi, R. Dolfini, A. Ereditato, G. Fiorillo, L. Grandi, et al., *New Astronomy Reviews* **49**, 265 (2005), ISSN 1387-6473, Sources and Detection of Dark Matter and Dark Energy in the Uni-

- verse, URL <http://www.sciencedirect.com/science/article/pii/S1387647305000370>.
- [7] D. Gastler, E. Kearns, A. Hime, L. C. Stonehill, S. Seibert, J. Klein, W. H. Lippincott, D. N. McKinsey, and J. A. Nikkel, Phys. Rev. C **85**, 065811 (2012), URL <https://link.aps.org/doi/10.1103/PhysRevC.85.065811>.
- [8] H. Cao, T. Alexander, A. Aprahamian, R. Avetisyan, H. O. Back, A. G. Cocco, F. DeJongh, G. Fiorillo, C. Galbiati, L. Grandi, et al. (SCENE Collaboration), Phys. Rev. D **91**, 092007 (2015), URL <https://link.aps.org/doi/10.1103/PhysRevD.91.092007>.
- [9] W. Creus, Y. Allkofer, C. Amsler, A. Ferella, J. Rochet, L. Scotto-Lavina, and M. Walter, J. Instrum. **10**, P08002 (2015), URL <http://stacks.iop.org/1748-0221/10/i=08/a=P08002>.
- [10] P. Agnes, I. Albuquerque, T. Alexander, A. Alton, D. Asner, H. Back, K. Biery, V. Bocci, G. Bonfini, W. Bonivento, et al., J. Instrum. **12**, P10015 (2017), URL <http://stacks.iop.org/1748-0221/12/i=10/a=P10015>.
- [11] P. Agnes, J. Dawson, S. De Cecco, A. Fan, G. Fiorillo, D. Franco, C. Galbiati, C. Giganti, T. N. Johnson, G. Korga, et al. (The ARIS Collaboration), Phys. Rev. D **97**, 112005 (2018), URL <https://link.aps.org/doi/10.1103/PhysRevD.97.112005>.
- [12] T. Doke, H. J. Crawford, A. Hitachi, J. Kikuchi, P. J. Lindstrom, K. Masuda, E. Shibamura, and T. Takahashi, Nucl. Inst. & Meth. in Phys. Res. A **269**, 291 (1988), ISSN 0168-9002, URL <http://www.sciencedirect.com/science/article/pii/0168900288908923>.
- [13] J. Lindhard, V. Nielsen, M. Scharff, and P. Thomsen, Mat. Fys. Medd. Dan. Vid. Selsk **33**, 1 (1963).
- [14] B. Lenardo, K. Kazkaz, A. Manalaysay, J. Mock, M. Szydagis, and M. Tripathi, IEEE Trans. Nucl. Sci. **62**, 3387 (2015), ISSN 0018-9499.
- [15] T. H. Joshi, S. Sangiorgio, A. Bernstein, M. Foxe, C. Hagmann, I. Jovanovic, K. Kazkaz, V. Mozin, E. B. Norman, S. V. Pereverzev, et al., Phys. Rev. Lett. **112**, 171303 (2014), URL <https://link.aps.org/doi/10.1103/PhysRevLett.112.171303>.
- [16] J. Thomas and D. A. Imel, Phys. Rev. A **36**, 614 (1987), URL <https://link.aps.org/doi/10.1103/PhysRevA.36.614>.
- [17] D.-M. Mei, Z.-B. Yin, L. Stonehill, and A. Hime, Astroparticle Phys. **30**, 12 (2008), ISSN 0927-6505, URL <http://www.sciencedirect.com/science/article/pii/S0927650508000765>.
- [18] T. Washimi, Ph.D. thesis, Waseda University, Japan (2018), (in Japanese).
- [19] M. Tanaka, in *Journal of Physics: Conference Series* (2013), vol. 469, p. 012012, URL <http://stacks.iop.org/1742-6596/469/i=1/a=012012>.
- [20] T. Washimi, M. Kimura, M. Tanaka, and K. Yorita, Nucl. Inst. & Meth. in Phys. Res. A **910**, 22 (2018), ISSN 0168-9002, URL <http://www.sciencedirect.com/science/article/pii/S0168900218311458>.
- [21] M. Kimura, K. Yorita, and M. Tanaka, in *Journal of Physics: Conference Series* (2019), vol. (TAUP2017), (accepted).
- [22] S. Agostinelli, J. Allison, K. Amako, J. Apostolakis, H. Araujo, P. Arce, M. Asai, D. Axen, S. Banerjee, G. Barrand, et al., Nucl. Inst. & Meth. in Phys. Res. A **506**, 250 (2003), ISSN 0168-9002, URL <http://www.sciencedirect.com/science/article/pii/S0168900203013688>.
- [23] J. Allison, K. Amako, J. Apostolakis, H. Araujo, P. A. Dubois, M. Asai, G. Barrand, R. Capra, S. Chauvie, R. Chytracek, et al., IEEE Trans. Nucl. Sci. **53**, 270 (2006), ISSN 0018-9499.
- [24] J. W. Boldeman, B. E. Clancy, and D. Culley, Nuclear Science and Engineering **93**, 181 (1986), URL <https://doi.org/10.13182/NSE86-2>.
- [25] E. Mendoza, D. Cano-Ott, T. Koi, and C. Guerrero, IEEE Trans. Nucl. Sci. **61**, 2357 (2014), ISSN 0018-9499.
- [26] E. Mendoza, D. Cano-Ott, C. Guerrero, and R. Capote, Tech. Rep., International Atomic Energy Agency (2012).
- [27] E. Mendoza and Cano-Ott, Tech. Rep., International Atomic Energy Agency (2018).
- [28] A. E. Robinson, Phys. Rev. C **89**, 032801 (2014), URL <https://link.aps.org/doi/10.1103/PhysRevC.89.032801>.
- [29] K.-H. Ackermann, M. Agostini, M. Allardt, M. Altmann, E. Andreotti, A. M. Bakalyarov, M. Balata, I. Barabanov, N. Barnabé Heider, M. nd Barros, L. Baudis, et al., Eur. Phys. J. C **73**, 2330 (2013), ISSN 1434-6052, URL <https://doi.org/10.1140/epjc/s10052-013-2330-0>.
- [30] R. Acciarri, S. Bansal, A. Friedland, Z. Djurcic, L. Rakotondravohitra, T. Xin, E. Mazzucato, C. Densham, E. Calvo, S. Li, et al. (DUNE Collaboration), FERMILAB-DESIGN-2016-01 (2016).
- [31] D. Akimov, J. Albert, P. An, C. Awe, P. Barbeau, B. Becker, V. Belov, M. Blackston, A. Bolozdynya, A. Brown, et al., *Coherent 2018 at the spallation neutron source*, e-print arXiv:physics.ins-det/1803.09183 (2018).